

Distribution Shifts at Scale: Out-of-distribution Detection in Earth Observation

Burak Ekim*

University of the Bundeswehr Munich

Girmaw Abebe Tadesse†

Microsoft AI for Good Research Lab

Caleb Robinson†

Microsoft AI for Good Research Lab

Gilles Hacheme

Microsoft AI for Good Research Lab

Michael Schmitt

University of the Bundeswehr Munich

Rahul Dodhia

Microsoft AI for Good Research Lab

Juan M. Lavista Ferres

Microsoft AI for Good Research Lab

Abstract

Training robust deep learning models is critical in Earth Observation, where globally deployed models often face distribution shifts that degrade performance, especially in low-data regions. Out-of-distribution (OOD) detection addresses this challenge by identifying inputs that differ from in-distribution (ID) data. However, existing methods either assume access to OOD data or compromise primary task performance, making them unsuitable for real-world deployment. We propose TARDIS, a post-hoc OOD detection method for scalable geospatial deployments. The core novelty lies in generating surrogate labels by integrating information from ID data and unknown distributions, enabling OOD detection at scale. Our method takes a pre-trained model, ID data, and WILD samples, disentangling the latter into surrogate ID and surrogate OOD labels based on internal activations, and fits a binary classifier as an OOD detector. We validate TARDIS on EuroSAT and xBD datasets, across 17 experimental setups covering covariate and semantic shifts, showing that it performs close to the theoretical upper bound in assigning surrogate ID and OOD samples in 13 cases. To demonstrate scalability, we deploy TARDIS on the Fields of the World dataset, offering actionable insights into pre-trained model behavior for large-scale deployments. The code is publicly available at <https://github.com/microsoft/geospatial-ood-detection>

*Work done while a resident at the Microsoft AI for Good Research Lab. Contact: burak.ekim@unibw.de

†Residency supervisor.

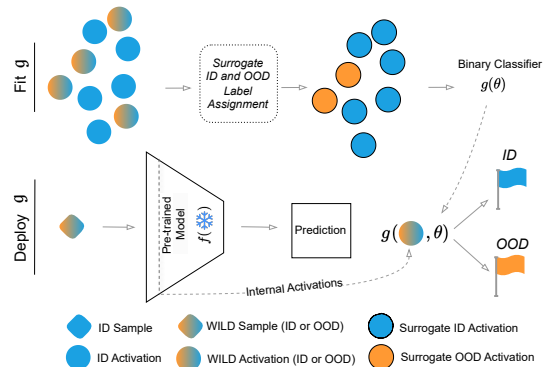


Figure 1. Illustration of the proposed method for OOD detection. Given a pre-trained model, a dataset of known ID samples, and WILD samples (containing both ID and OOD data), the method assigns surrogate ID or OOD labels to each WILD sample and fits a binary classifier g (top row). During deployment, the classifier g uses internal activations to predict whether an unseen sample is ID or OOD (bottom row).

1. Introduction

Deep learning (DL) models have demonstrated remarkable capabilities across various domains but often exhibit overconfidence in their predictions, even when confronted with data that diverges from their training distribution [10, 19, 25]. This overconfidence arises from the assumption that inference data will follow the same independent and identically distributed (*i.i.d.*) properties as the training data. However, in real-world applications, this

closed-world assumption [8, 14] is frequently violated by test-time distribution shifts (e.g., lighting or angle variations, different devices or sensors) that can significantly degrade model performance and harm generalization. To address this, it is critical for predictive models to detect when new observations fall outside the training distribution, a task known as out-of-distribution (OOD) detection. Differentiating OOD from in-distribution (ID) samples is particularly challenging, partly due to the poor calibration of neural networks [6, 18]. This degradation poses a critical challenge, especially in applications where incorrect predictions can have severe consequences. In Earth Observation (EO), specifically with satellite imagery, distribution shifts are even more common due to variability in sensor types, acquisition angles, temporal changes, spatial variations, and landscape alterations caused by events such as natural disasters. This variability necessitates unique, tailored approaches for satellite imagery [21]. The nature of distribution shifts between training and inference data can be classified as near-distribution or far-distribution shifts, each posing unique challenges. For example, a model trained on data from a certain season and region may perform poorly when applied to other seasons in the same region or the same season in different regions [13], representing a far-distribution shift. Even models trained on data covering multiple seasons and regions may perform suboptimally under specific acquisition or atmospheric conditions, such as cloud cover, sensor faults, or artifacts, indicative of a near-distribution shift.

Despite the critical importance of robust models in Earth Observation (EO), only a few studies address OOD detection in this domain [1, 3, 5]. These studies typically assume access to test-time distributions, rely on closed-set assumptions, and often sacrifice model performance on in-distribution tasks. This highlights the need for tailored OOD detection methods suited for large-scale EO deployment.

A further challenge arises when applying geospatial models globally. Many geospatial products, while measuring the same ground realities with high coverage, exhibit low levels of agreement [2]. Additionally, global geospatial models often suffer significant performance drops in low-data regions, such as sub-Saharan Africa [12]. These issues emphasize the need for global models equipped to detect OOD samples during inference.

OOD detection capabilities in real-world applications enhance model reliability by identifying when input data deviates from the training distribution. They also support resource allocation and targeted data collection by pinpointing areas where the model may underperform, effectively guiding both computational and human resources. Additionally, OOD detection enables real-time adjustments, allowing models to remain reliable in dynamic conditions. This approach supports a human-in-the-loop strategy for

critical decisions, fostering trust, transparency, and accountability. Overall, OOD detection is essential for managing large-scale EO deployments effectively.

In this paper, we begin with an essential observation: OOD samples can trigger internal activation patterns that diverge from those of ID samples. Building on this insight and recognizing the challenges of deploying geospatial models at scale, we introduce the following key contributions:

- We propose TARDIS (Test-time Addressing of Distribution Shifts at Scale), a post-hoc OOD detection method that preserves the model’s performance on the main task and operates without requiring access to unknown test-time near-distribution shifts.
- We evaluate TARDIS on EuroSAT, a patch-classification dataset, and xBD, a semantic segmentation dataset, examining both covariate and semantic shifts across 16 experimental setups. For covariate shifts, we introduce geographical variance (spatial changes), temporal variance (seasonal changes), and environmental variance (land-cover or disaster type changes). Semantic shifts are introduced by withholding a class during training and exclusively testing on that class, thus presenting new semantic categories.
- We demonstrate that TARDIS can be deployed at scale, providing actionable insights into the trustworthiness and robustness of geospatial models in real-world scenarios.

2. Related Works

Our method lies at the intersection of two notable categories of OOD detection methods: scoring functions and activation manipulation. Scoring functions assign a numerical score to each input, reflecting its alignment with ID samples based on the model’s output. Maximum Softmax Probability (MSP) [10] detects OOD samples by assessing the softmax confidence score, assuming that low confidence indicates OOD samples. The Out-of-Distribution detector for Neural networks (ODIN) [16] enhances MSP by applying input perturbations and temperature scaling to improve ID-OOD separation. The Mahalanobis score [15] calculates the distance between input features and class means in feature space, flagging inputs far from these means as OOD. The energy score [17] evaluates the model’s energy function to assess the likelihood of an input belonging to the ID distribution. Another category of OOD detection methods manipulates the internal activations of a pre-trained model to improve detection performance. ReAct [24] identifies differences in activation patterns of the penultimate layer between ID and OOD samples, enhancing separation by clipping activations at an upper limit. DICE [23] applies weight sparsification on a specific layer to further distinguish ID from OOD data and, when combined with ReAct, can enhance detection performance. Activation Shap-

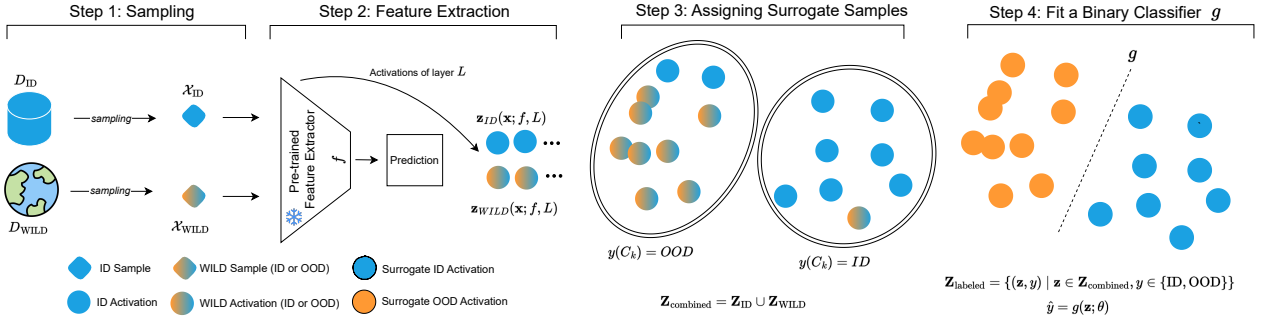


Figure 2. The proposed framework consists of four key steps: (1) Sampling in-distribution (ID) and WILD samples; (2) Extracting internal activations from a pre-trained model f for both ID and WILD samples; (3) Clustering the combined feature space and labeling WILD samples as surrogate-ID or surrogate-OOD; (4) Fitting a binary classifier g on the labeled feature representations to distinguish between ID and OOD samples. The classifier g , during deployment, flags out-of-distribution inputs.

ing [4] prunes a portion of an input sample’s activations and slightly adjusts the remaining activations; when paired with the energy score, this approach has been shown to outperform contemporary OOD methods. Neuron Activation Patterns (NAP) [20] extracts, downsamples, and binarizes activation patterns from convolutional layers, computing the smallest Hamming distance between binarized test and training patterns. This distance provides a measure of model uncertainty, aiding in OOD detection.

Both scoring functions and activation-based strategies face notable challenges in dynamic, real-world environments. Scoring functions, while maintaining ID accuracy, struggle with OOD detection due to their reliance on static data distributions, an assumption rarely valid in practice. Activation-based methods, though effective, often compromise ID task performance and rely on hyperparameters tuned with hypothetical or substitute OOD samples. This reliance limits their effectiveness under evolving test-time conditions and shifting distributions.

The task of OOD detection is inherently challenging, and the EO domain is no exception due to the diverse and heterogeneous nature of satellite imagery. Despite the critical importance of OOD detection in EO, this area remains relatively underexplored, with only a limited number of studies addressing the issue. One such study develops a Dirichlet Prior Network to quantify distributional uncertainty in DL models for satellite image analysis [5]. This method assumes Dirichlet distributions for ID samples and employs various setups where classes, color channels, and environmental features are alternately treated as ID or OOD. Another study frames anomaly detection as a cumulative open-set detection and location separation task [3]. This approach also uses a Dirichlet prior, similar to the first study, to expand the representation space between ID (normal) and

OOD (anomalous) samples by predicting the anticipated categorical distribution. The method is suitable for scenarios where pre-event images are either unavailable, subject to radiation differences, or not sufficiently recent to aid in detection.

In this paper, we do not aim to optimize OOD detection performance but instead propose a method designed for real-world applications where the distribution is unknown, maintaining ID task performance is critical, and computationally expensive methods are impractical. Our focus is on handling near-distribution shifts, where data variations stem from the same satellite sources but exhibit changes over time, geography, or environmental factors. This contrasts with far-distribution shifts, where variations arise from entirely different data sources, such as different satellite models or natural images.

3. Problem Formulation

Let \mathcal{X} represent the set of all possible data the model may encounter, and \mathcal{Y} the set of class labels. The dataset on which a model is trained is defined as in-distribution (ID), denoted $D_{ID} \subset \mathcal{X}_{ID} \times \mathcal{Y}$. During inference, however, the model may encounter data from an unknown distribution, referred to as the WILD dataset $D_{WILD} \subset \mathcal{X}_{WILD}$, which may contain both ID and OOD samples.

We assume a pre-trained neural network $f : \mathcal{X} \rightarrow \mathbb{R}^{|\mathcal{Y}|}$, trained on D_{ID} , and our objective is to distinguish between ID and OOD samples within D_{WILD} . The network f extracts features $\mathbf{z} \in \mathbb{R}^F$, where F is the dimensionality of the feature space. Specifically, we fit a binary classifier $g : \mathbb{R}^F \rightarrow \{0, 1\}$, parametrized by θ , that operates on these features \mathbf{z} for a given sample in \mathcal{X}_{WILD} . We define $g(\mathbf{z}; \theta) = 0$ if $\mathbf{x} \sim D_{ID}$, and $g(\mathbf{z}; \theta) = 1$ if $\mathbf{x} \sim D_{OOD}$.

4. Method

Fitting a classifier to distinguish between in-distribution (ID) and out-of-distribution (OOD) samples typically requires known ID and OOD labels, which is impractical in real-world deployments. This creates a need for surrogate ID and OOD labels for samples with unknown distributions, which we refer to as WILD samples. Our method, illustrated in Figure 1, operates with a given model, a set of known ID samples, and a set of WILD samples. It generates surrogate ID and OOD labels for the WILD samples, which are then used to train a binary classifier that can classify the distribution of incoming samples.

First, we sample M in-distribution samples from the ID set and N WILD samples from the WILD set. Next, we pass both the ID and WILD samples through the frozen pre-trained model and extract activations from a specified layer. A pooling operation is applied to perform spatial downsampling, transforming the activations into one-dimensional vectors and combining the downsampled features. We then use k-means clustering to partition the combined features into K clusters. For each cluster, we calculate the proportion of ID samples and assign surrogate labels based on a threshold T : if the proportion of ID samples in the cluster is greater than or equal to T , the surrogate label is 0; otherwise, it is 1.

Here, $y_{\text{sur}}(\mathbf{z})$ denotes the surrogate label: 0 for surrogate ID and 1 for surrogate OOD. With this labeled dataset, we fit a binary classifier $g(\mathbf{z}; \theta)$, which maps a sample to a predicted label. During deployment, for a sample of unknown distribution, we perform activation extraction and classification as follows: $\hat{y} = g(\text{Downsample}(f(\mathbf{x})); \theta)$. The output can be interpreted as probability scores, allowing it to quantify the magnitude of domain shift or thresholded to produce binary values (0 for in-distribution and 1 for out-of-distribution).

Surrogate Label Assignment. The core novelty of TARDIS lies in its surrogate labeling generation step, which enables us to assign labels to WILD samples based on their proximity to ID samples in feature space. The assumption is that ID and OOD features are sufficiently distinct to allow effective separation through clustering. Specifically, we use k-means clustering to label WILD samples as surrogate OOD if WILD samples outnumber ID samples in a cluster, and as surrogate ID otherwise. Without access to true OOD data, ID samples serve as an indirect benchmark for distinguishing between ID and WILD samples. To optimize this process, we tune the number of clusters K and threshold T by balancing three objectives: entropy (to encourage homogeneity within clusters and distinct groups of surrogate labels), correct ID proportion (to maximize accurate identification of ID samples), and incorrect ID proportion (to minimize the misclassification of ID samples as OOD). The combined objective function mini-

mizes average entropy and the misclassification rate of ID samples while maximizing correct ID classification, resulting in well-separated and accurately labeled groups.

Figure 2 illustrates our method. First, ID samples are drawn from the model’s training set, while WILD samples, representing unknown distributions, are sourced from satellite images taken at any location and time (Step 1). Both ID and WILD samples are passed through a pre-trained model, and internal activations are extracted from a specified layer (Step 2). Using these activations, we assign surrogate labels to WILD samples, categorizing them as surrogate ID or surrogate OOD (Step 3). This surrogate labeling, central to our approach, decomposes WILD samples based on their distributional alignment with ID samples. Finally, these labeled feature representations are used to train a binary classifier that, during deployment, outputs probability scores or thresholded 0/1 predictions to classify samples as either ID or OOD (Step 4).

5. Experimental Setup

In this section, we describe the experimental setups designed to evaluate TARDIS under controlled distribution shifts, which mimic real-world geospatial deployment challenges. Specifically, we use the EuroSAT [9] dataset for patch-level classification and the xBD [7] dataset for semantic segmentation. EuroSAT contains 27,000 labeled images across ten land use and land cover classes: Annual Crop, Forest, Herbaceous Vegetation, Highway, Industrial, Pasture, Permanent Crop, Residential, River, and Sea/Lake. The xBD dataset includes over 1 million labeled samples for building damage assessment from satellite imagery, covering multiple disaster types such as hurricanes, floods, and wildfires. For our experiments, we formulate xBD as a building footprint segmentation task with two classes (building footprint and background). EuroSAT and xBD provide a suitable test-bed for our OOD method due to their differences in volume, task, sensor type, geospatial distribution, and temporal and spatial characteristics, allowing a thorough evaluation under conditions commonly encountered in geospatial deployments.

To introduce controlled distribution shifts, we reformulate the train, validation, and test splits of EuroSAT and xBD so that the model, when trained on the modified training set and evaluated on the adjusted test set, encounters shifts similar to those seen in geospatial model deployments. We categorize these shifts as covariate shift and semantic shift. Covariate shift occurs when the input data distribution changes between training and testing. This can introduce selection bias, as covariates in the training set may still appear in the test set to some extent, potentially skewing robustness evaluation. To address this, we also introduce semantic shift experiments where a class is held out during testing, creating an unseen semantic class. For our

Table 1. Overview of experimental setups for evaluating TARDIS under controlled distribution shifts. The table details the covariate and semantic shift scenarios, including the dataset used, split method, and the composition of the ID and out-of-distribution OOD sets. All conditions are post-event except where specified.

Type	Dataset	Split Method	ID (Training Set)	OOD (Test Set)
Covariate Shift	EuroSAT	Spatial Split (Longitude)	West Europe	East Europe
		Similar Disasters - Distant Locations	Nepal Flooding	Midwest Flooding
	xBD	Similar Disasters - Nearby Locations	Santa Rosa Wildfire	Woolsey Fire
		Different Disasters - Distant Locations	Hurricane Matthew	Nepal Flooding
		Different Disasters - Nearby Locations	Hurricane Matthew	Mexico Earthquake
		Temporal	Portugal Wildfire (Pre-Disaster)	Portugal Wildfire
Semantic Shift	EuroSAT	Unseen Class (Repeated for 10 Classes)	9 out of 10 classes (e.g., Annual Crop, Forest, Herbaceous Vegetation, Highway, Industrial, Pasture, Permanent Crop, Residential, River)	1 holdout class (e.g., Sea/Lake)

experiments, covariate shifts include spatial variance (varying spatial locations), temporal variance (varying time of data collection), and environmental variance (varying land-cover or disaster types). For semantic shifts in the EuroSAT dataset, we train the model on nine out of ten classes and test on the holdout class, repeating this process so that each class serves as the holdout class once. Details of the experimental setups are provided in Table 1.

The setups described above assume clear definitions of ID (training set) and OOD (test set), which presupposes access to test-time distribution shifts, an assumption that is not feasible in real-world deployments. To evaluate our method’s performance under unknown test-time distribution shifts, we fit and evaluate the binary classifier g in two distinct ways. In the first approach, we bypass surrogate label assignment (Step 3 in Figure 2), using the well-defined ID and OOD samples to fit and evaluate the classifier, referred to as g_{oracle} . In the second approach, we treat the OOD labels in the test set as unknown, simulating real-world conditions where these labels are unavailable. This method uses surrogate label assignment to reassign unknown labels into surrogate ID and surrogate OOD. Parameter estimation and evaluation on these reassigned labels yield a classifier denoted as g^* , representing our proposed method. The underlying assumption is that g_{oracle} provides an upper bound on performance for g^* , as g_{oracle} is trained with clearly separated ID and OOD samples, whereas g^* is trained on surrogate ID and surrogate OOD samples that are

generated through our surrogate label assignment process.

6. Experimental Results

In this section, we present the ablation studies and discuss the results of the surrogate sample assignment benchmark, where we evaluate the performance of g^* . Note that ID task performance is not reported, as it remains unaffected by our method.

Ablation Studies. We conduct benchmark studies on the g_{oracle} classifier to explore the factors influencing TARDIS’s ability to detect test-time distribution shifts. This ability depends significantly on the layer from which internal activations are extracted and the downsampling method applied. To address this, we test different layers and compare their performance. For downsampling, we experiment with several methods, including mean and standard deviations, average pooling, max pooling, and PCA-based reduction. The max pooling-based downsampling method achieves the highest performance, likely due to its ability to retain the most salient activation patterns, which we argue is important for effective OOD detection. After selecting the optimal layer and downsampling method, we evaluate various classifiers: KNeighbors, GaussianNB, DecisionTree, ExtraTrees, LogisticRegression, SVC, RandomForestUnbalanced, RandomForest, AdaBoost, and GradientBoosting. Results indicate that Logistic Regression provides the best tradeoff between classification performance and wall time. We then compare g^* to g_{oracle} as we tune the parameters K

Table 2. Performance metrics comparing the oracle classifier g_{oracle} and the surrogate classifier g^* for EuroSAT and xBD datasets across various experimental setups. The g_{oracle} classifier acts as an upper bound for the g^* , which is the proposed method. The † notation indicates that over 10 measurements, the difference was not found to be statistically significant ($p < 0.05$). All conditions are post-event except where specified.

Type	Dataset	OOD (Test Set)	ID (Training Set)	AUROC↑		FPR95↓	
				g_{oracle}	g^*	g_{oracle}	g^*
Covariate Shift	EuroSAT	Eastern Europe	Western Europe	$0.91 \pm 0.04^\dagger$	$0.89 \pm 0.06^\dagger$	$0.32 \pm 0.11^\dagger$	$0.37 \pm 0.10^\dagger$
		Midwest Flooding	Nepal Flooding	$1.00 \pm 0.00^\dagger$	$1.00 \pm 0.00^\dagger$	$0.01 \pm 0.02^\dagger$	$0.01 \pm 0.02^\dagger$
	xBD	Woolsey Fire	Santa Rosa Wildfire	$0.94 \pm 0.02^\dagger$	$0.93 \pm 0.02^\dagger$	$0.23 \pm 0.08^\dagger$	$0.27 \pm 0.09^\dagger$
		Nepal Flooding	Hurricane Matthew	0.99 ± 0.01	0.98 ± 0.01	$0.06 \pm 0.04^\dagger$	$0.07 \pm 0.02^\dagger$
		Mexico Earthquake	Hurricane Matthew	$0.96 \pm 0.02^\dagger$	$0.94 \pm 0.03^\dagger$	$0.11 \pm 0.05^\dagger$	$0.19 \pm 0.08^\dagger$
		Portugal Wildfire (Pre)	Portugal Wildfire	0.99 ± 0.00	0.95 ± 0.01	0.06 ± 0.04	0.23 ± 0.20
		Santa Rosa Wildfire	Woolsey Fire	$0.94 \pm 0.02^\dagger$	$0.93 \pm 0.02^\dagger$	$0.23 \pm 0.08^\dagger$	$0.27 \pm 0.09^\dagger$
Semantic Shift	EuroSAT	Remaining 9 classes	Forest	$0.99 \pm 0.01^\dagger$	$0.97 \pm 0.02^\dagger$	$0.08 \pm 0.04^\dagger$	$0.08 \pm 0.05^\dagger$
			Herbaceous Vegetation	$0.93 \pm 0.03^\dagger$	$0.88 \pm 0.07^\dagger$	$0.26 \pm 0.11^\dagger$	$0.29 \pm 0.14^\dagger$
			Highway	$0.63 \pm 0.08^\dagger$	$0.56 \pm 0.06^\dagger$	$0.78 \pm 0.13^\dagger$	$0.88 \pm 0.10^\dagger$
			Industrial	$0.97 \pm 0.02^\dagger$	$0.96 \pm 0.02^\dagger$	$0.13 \pm 0.14^\dagger$	$0.22 \pm 0.07^\dagger$
			Pasture	0.98 ± 0.01	0.95 ± 0.01	$0.09 \pm 0.06^\dagger$	$0.28 \pm 0.19^\dagger$
			Permanent Crop	$0.92 \pm 0.03^\dagger$	$0.89 \pm 0.03^\dagger$	$0.26 \pm 0.08^\dagger$	$0.33 \pm 0.11^\dagger$
			Residential	$0.87 \pm 0.03^\dagger$	$0.82 \pm 0.06^\dagger$	$0.46 \pm 0.21^\dagger$	$0.43 \pm 0.15^\dagger$
			River	0.87 ± 0.04	0.81 ± 0.06	$0.44 \pm 0.14^\dagger$	$0.57 \pm 0.10^\dagger$
			Sea-Lake	$1.00 \pm 0.00^\dagger$	$1.00 \pm 0.00^\dagger$	$0.00 \pm 0.00^\dagger$	$0.00 \pm 0.00^\dagger$
Annual Crop	$0.92 \pm 0.03^\dagger$	$0.91 \pm 0.04^\dagger$	$0.25 \pm 0.10^\dagger$	$0.32 \pm 0.16^\dagger$			

and T required for surrogate label assignment. To determine K and T , we use a Tree-structured Parzen Estimator for sampling. Specifically, we set the search boundaries for K (the number of clusters) between 2 and $0.3 \times M$, where M is the total number of samples, and for T (the fraction of in-distribution samples within a cluster, below which the cluster is labeled as surrogate OOD) between 0.01 and 0.2. These values were empirically determined based on preliminary tuning for optimal performance. We then run 20 independent experiments and select the best-performing (K, T) pair. Fixing T based on the hyperparameter search results, we observe a recurring pattern that enables us to fix K to $0.3 \times M$ across all setups. This choice is driven by the observation that the classifier g^* reaches performance levels close to g_{oracle} when K is set to 30% of the total training samples. This trend holds across both datasets, with the xBD disaster scenario (semantic shift) and EuroSAT Pasture experiment (covariate shift) showing similar behavior. In both cases, classifier performance improves as more clusters are incorporated, approaching the performance of g_{oracle} . We present the results of TARDIS across these controlled distribution shifts in the Supplementary Material.

Surrogate Sample Assignment Benchmark. The quantitative results for g^* and g_{oracle} across 16 experimental setups are shown in Table 2. Across all setups, g^* closely matches the performance of g_{oracle} , which represents the upper bound for our method. Specifically, in 13 setups for AUROC and 17 setups for FPR95, the difference between g^* and g_{oracle} is not statistically significant. In the remaining setups, while a small performance difference exists, the proposed method largely recovers the theoretical upper bound. This minimal, and often statistically insignificant, performance gap demonstrates that TARDIS can assign surrogate ID and OOD labels with high performance, even without access to test-time distribution during training.

A key takeaway from these experiments is the method’s ability to disentangle WILD samples with unknown test-time distributions into surrogate ID and OOD samples. Notably, under unknown distribution settings, it achieves performance comparable to cases with known ID and OOD labels, highlighting its strength in reliable OOD detection without prior distribution knowledge, making it suitable for real-world geospatial applications.

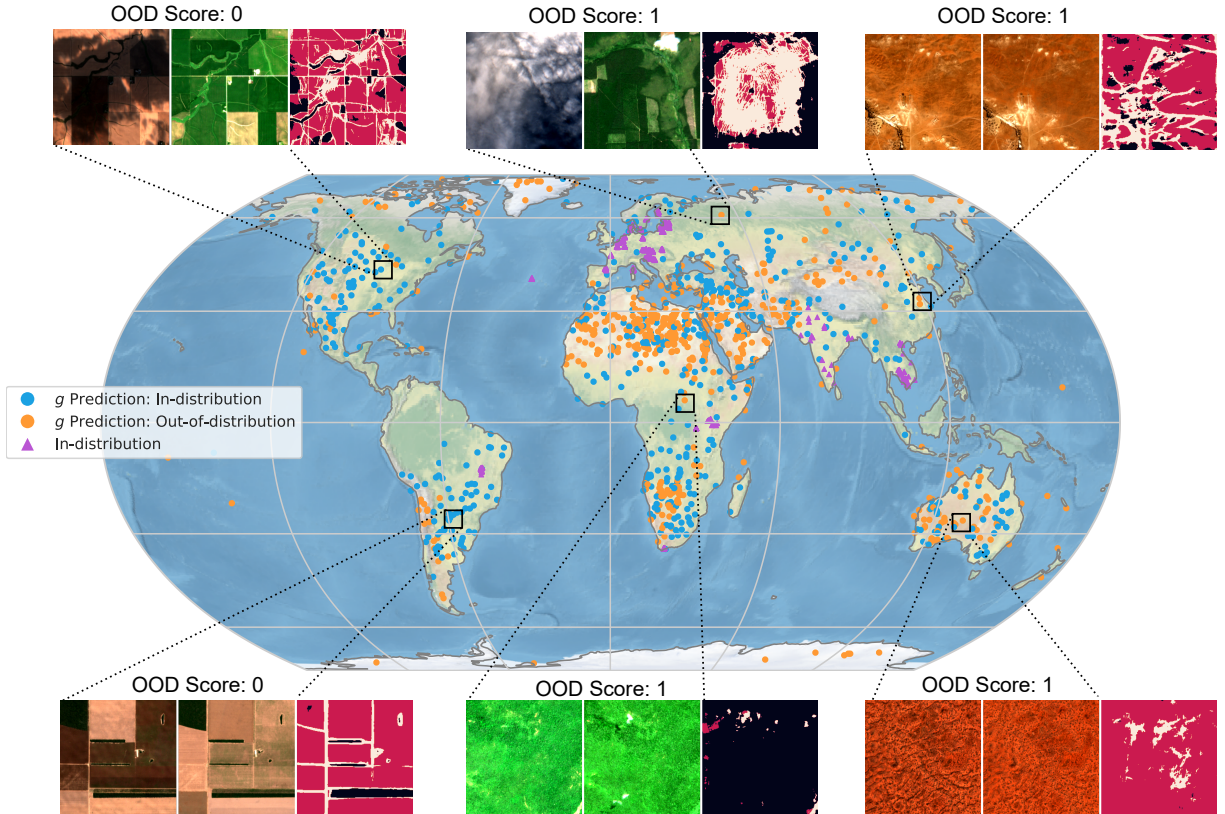


Figure 3. Geographical distribution of ID and WILD sets, containing 500 and 1200 samples, respectively. The ID set is sampled from the FTW dataset training set, while the WILD set is randomly sampled from the Microsoft Planetary Computer. Each Sentinel-2 patch, provided in two different time frames (planting and harvesting). The model f takes both Sentinel-2 images from different seasons as input, and the predictions are shown on the right. The bar indicates the probability output of g for each input pair, with a higher probability (closer to 1) suggesting a higher likelihood of the pair being OOD. On the map, probability values are thresholded at 0.5.

7. OOD Detection Goes Global: Real-World Deployment

We use the Fields of the World (FTW) pre-trained models [11] to demonstrate the capabilities of TARDIS in a large-scale deployment scenario. FTW is a geographically diverse dataset designed for agricultural field segmentation, covering 24 regions across Europe, Africa, Asia, and South America: Austria, Belgium, Brazil, Cambodia, Corsica, Croatia, Denmark, Estonia, Finland, France, Germany, India, Kenya, Latvia, Lithuania, Luxembourg, Netherlands, Portugal, Rwanda, Slovakia, Slovenia, South Africa, Spain, Sweden, and Vietnam. The dataset contains approximately 70,000 samples, each consisting of multi-date, multi-spectral Sentinel-2 satellite patches paired with three-class semantic segmentation masks (field, field boundary, and background). The task involves segmenting these classes using a pair of Sentinel-2 images — one for the planting season and one for the harvesting season — as input. Field boundary data is crucial for global agricultural

monitoring, however training large scale models to segment field boundaries from satellite imagery presents significant challenges due to the geographic diversity of fields, varying crop cycles, and agro-climatic conditions, all of which introduce substantial distribution shifts. This complexity, along with corresponding distribution shifts found in real world imagery, makes the FTW dataset ideal for testing TARDIS’s ability to diagnose model performance during inference. Additionally, the multi-date nature of the dataset is particularly suitable for evaluating segmentation models that must handle spatiotemporal variations in satellite imagery.

Sampling ID Set. To form the ID set, we sample 50 patches from each country represented in the training set, ensuring a geographically diverse ID dataset that closely matches the data on which the model was originally trained.

Sampling WILD Set. We collect multispectral Sentinel-2 satellite images using the Microsoft Planetary Computer [22], which is freely accessible. The images are processed to Level-2A (bottom-of-atmosphere) and stored

in cloud-optimized GeoTIFF (COG) format. We use four spectral bands: Red (B04), Green (B03), Blue (B02), and Near-Infrared (B08), each with a spatial resolution of 10 meters per pixel. We randomly query 1200 Sentinel-2 scenes from those over land and with cloud coverage $< 10\%$. Then, from each scene, we generate random patches of shape $256 \times 256 \times 4$ pixels (filtering out samples with $\geq 10\%$ zero or NaN pixels) and query both the planting and harvesting seasons for the same locations. The planting and harvesting dates are fixed based on the hemisphere: April 1 to June 30 and September 1 to November 30 for the Northern Hemisphere, and October 1 to December 31 and March 1 to May 31 for the Southern Hemisphere. The two patches are concatenated along the channel dimension, resulting in a patch of shape $256 \times 256 \times 8$ pixels. Following the pre-trained model’s convention, the concatenated patch is upsampled by a factor of 2 to $512 \times 512 \times 8$, processed by the model, and then downsampled back to the original dimensions. For surrogate label assignment, we fix the hyperparameters K and T to 0.3×1200 and 0.1 , respectively, as suggested by the benchmark study.

The geographical distribution of ID and WILD samples is illustrated in Figure 3, where WILD samples are further classified into ID and OOD categories. A notable pattern is that samples located in arid biomes — such as the deserts in Inner Australia, the Sahara, and Patagonia — and polar regions, including Icelandic glaciers and the South Pole, are more likely to be assigned as OOD. This can be attributed to the ID samples predominantly representing mesic environments, which are areas with moderate moisture levels and managed landscapes suitable for agriculture. In contrast, arid biomes and polar regions exhibit extreme environmental conditions that differ markedly from the mesic environments of the ID samples. This ecological dissimilarity results in these biomes being classified as surrogate OOD, highlighting the model’s sensitivity to environmental context and distribution shifts.

To evaluate the scalability of our method, we measure the time required to classify the internal activation of a WILD sample as surrogate ID or OOD using the classifier g , implemented as a logistic regressor. An input patch of shape 256×256 pixels, with a spatial resolution of 10 meters per pixel, covers an area of 6.5536 km^2 and takes 0.003 seconds to process. Applied to the entirety of mainland Africa, which spans $29.77 \times 10^6 \text{ km}^2$, the method could be deployed on a single CPU in approximately 15 days. In a distributed GPU setup, this process could be completed within hours (a fraction of the time required for f model inference over a similar area). This is crucial as such a model would allow practitioners to see, spatially, where the field boundary model itself is performing in distribution versus not (and where the corresponding outputs are likely irrelevant). These results demonstrate the practicality of the proposed method for deployment in low-data regimes, where

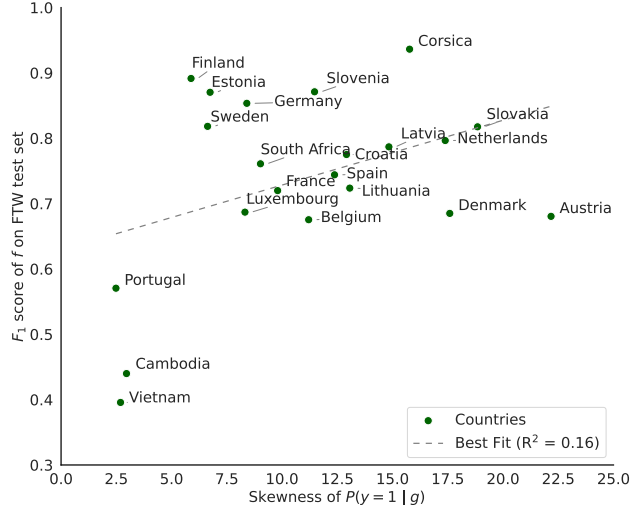


Figure 4. Relationship between model performance and OOD score skewness. The figure illustrates the correlation between low performance of the f model on the FTW test set and low skewness in the OOD classifier g ’s score distribution. When the f model performs poorly, the OOD classifier g produces more OOD scores, as reflected by lower skewness values.

geospatial models are typically less robust, and highlight its potential for improving model understanding in these challenging settings.

We further evaluate the reliability of the OOD classifier g on the training set by comparing the performance of the f model on the FTW dataset’s test set with the probability scores from g . We observe a correlation between the performance of the f model on the test set and low skewness in the output of g . This indicates that when the f model performs poorly, the OOD classifier g reflects this by producing unimodal OOD scores, as shown by low skewness values (see Figure 4) for countries such as Portugal, Cambodia, and Vietnam.

8. Conclusion

We present TARDIS, which effectively assigns surrogate ID or OOD labels to samples with unknown distributions by clustering the representation space. These surrogate labels are used to train a binary classifier for OOD detection. We do not aim to optimize OOD detection performance but instead propose a method designed for real-world applications where the distribution is unknown, maintaining ID task performance is critical, and computationally expensive methods are impractical. It achieves performance close to the theoretical upper limit in assigning surrogate ID and OOD samples in 13 out of 17 experiments. We demonstrate TARDIS can be deployed at scale, with the potential to enhance the robustness and trustworthiness of geospatial models as well as provide insights into distribution shifts in global applications.

References

- [1] Georges Le Bellier and Nicolas Audebert. Detecting out-of-distribution earth observation images with diffusion models, 2024. 2
- [2] Heather R Chamberlain, Edith Darin, Wole Ademola Adewole, Warren C Jochem, Attila N Lazar, and Andrew J Tatem. Building footprint data for countries in africa: to what extent are existing data products comparable? *Computers, Environment and Urban Systems*, 110:102104, 2024. 2
- [3] Mihai Coca, Iulia Coca Neogoe, and Mihai Datcu. Hybrid dnn-dirichlet anomaly detection and ranking: Case of burned areas discovery. *IEEE Transactions on Geoscience and Remote Sensing*, 60:1–16, 2022. 2, 3
- [4] Andrija Djuricic, Nebojsa Bozanic, Arjun Ashok, and Rosanne Liu. Extremely simple activation shaping for out-of-distribution detection. In *The Eleventh International Conference on Learning Representations*, 2023. 3, 2
- [5] Jakob Gawlikowski, Sudipan Saha, Anna Kruspe, and Xiao Xiang Zhu. Out-of-distribution detection in satellite image classification, 2021. 2, 3
- [6] Chuan Guo, Geoff Pleiss, Yu Sun, and Kilian Q Weinberger. On calibration of modern neural networks. In *International conference on machine learning*, pages 1321–1330. PMLR, 2017. 2
- [7] Ritwik Gupta, Richard Hosfelt, Sandra Sajeev, Nirav Patel, Bryce Goodman, Jigar Doshi, Eric Heim, Howie Choset, and Matthew Gaston. xbd: A dataset for assessing building damage from satellite imagery, 2019. 4, 1
- [8] Kaiming He, Xiangyu Zhang, Shaoqing Ren, and Jian Sun. Delving deep into rectifiers: Surpassing human-level performance on imagenet classification. In *Proceedings of the IEEE International Conference on Computer Vision (ICCV)*, 2015. 2
- [9] Patrick Helber, Benjamin Bischke, Andreas Dengel, and Damian Borth. Eurosat: A novel dataset and deep learning benchmark for land use and land cover classification, 2019. 4, 1
- [10] Dan Hendrycks and Kevin Gimpel. A baseline for detecting misclassified and out-of-distribution examples in neural networks. *arXiv preprint arXiv:1610.02136*, 2016. 1, 2
- [11] Hannah Kerner, Snehal Chaudhari, Aninda Ghosh, Caleb Robinson, Adeel Ahmad, Eddie Choi, Nathan Jacobs, Chris Holmes, Matthias Mohr, Rahul Dodhia, Juan M. Lavista Ferres, and Jennifer Marcus. Fields of the world: A machine learning benchmark dataset for global agricultural field boundary segmentation, 2024. 7
- [12] Hannah Kerner, Catherine Nakalembe, Adam Yang, Ivan Zvonkov, Ryan McWeeny, Gabriel Tseng, and Inbal Becker-Reshef. How accurate are existing land cover maps for agriculture in sub-saharan africa? *Scientific Data*, 11(1):486, 2024. 2
- [13] Hannah Kerner, Saketh Sundar, and Mathan Satish. Multi-region transfer learning for segmentation of crop field boundaries in satellite images with limited labels. *arXiv preprint arXiv:2404.00179*, 2024. 2
- [14] Alex Krizhevsky, Ilya Sutskever, and Geoffrey E Hinton. Imagenet classification with deep convolutional neural networks. In *Advances in Neural Information Processing Systems*. Curran Associates, Inc., 2012. 2
- [15] Kimin Lee, Kibok Lee, Honglak Lee, and Jinwoo Shin. A simple unified framework for detecting out-of-distribution samples and adversarial attacks, 2018. 2
- [16] Shiyu Liang, Yixuan Li, and R. Srikant. Enhancing the reliability of out-of-distribution image detection in neural networks, 2020. 2
- [17] Weitang Liu, Xiaoyun Wang, John D. Owens, and Yixuan Li. Energy-based out-of-distribution detection, 2021. 2
- [18] Matthias Minderer, Josip Djolonga, Rob Romijnders, Frances Hubis, Xiaohua Zhai, Neil Houlsby, Dustin Tran, and Mario Lucic. Revisiting the calibration of modern neural networks, 2021. 2
- [19] Anh Nguyen, Jason Yosinski, and Jeff Clune. Deep neural networks are easily fooled: High confidence predictions for unrecognizable images. In *Proceedings of the IEEE conference on computer vision and pattern recognition*, pages 427–436, 2015. 1
- [20] Bartłomiej Olber, Krystian Radlak, Adam Popowicz, Michal Szczepankiewicz, and Krystian Chachula. Detection of out-of-distribution samples using binary neuron activation patterns, 2023. 3, 2
- [21] Esther Rolf, Konstantin Klemmer, Caleb Robinson, and Hannah Kerner. Mission critical–satellite data is a distinct modality in machine learning. *arXiv preprint arXiv:2402.01444*, 2024. 2
- [22] Microsoft Open Source, Matt McFarland, Rob Emanuele, Dan Morris, and Tom Augspurger. microsoft/planetarycomputer: October 2022, 2022. 7
- [23] Yiyu Sun and Yixuan Li. Dice: Leveraging sparsification for out-of-distribution detection, 2022. 2
- [24] Yiyu Sun, Chuan Guo, and Yixuan Li. React: Out-of-distribution detection with rectified activations, 2021. 2
- [25] Christian Szegedy, Wojciech Zaremba, Ilya Sutskever, Joan Bruna, Dumitru Erhan, Ian Goodfellow, and Rob Fergus. Intriguing properties of neural networks. *arXiv preprint arXiv:1312.6199*, 2013. 1

Distribution Shifts at Scale: Out-of-distribution Detection in Earth Observation

Supplementary Material

In this supplement, we first detail the datasets and models used, followed by a discussion of the introduced distribution shifts and their design rationale. Next, we evaluate the impact of various design choices, including layer selection, downsampling methods, classifiers, and surrogate label assignment hyperparameters. Finally, we present additional experimental results with detailed visualizations and performance metrics to provide deeper insights into the behavior and performance of our method.

9. Datasets and Model Details

9.1. EuroSAT

EuroSAT [9] is a scene classification dataset derived from Sentinel-2 satellite images, covering various locations across Europe. It contains 27,000 images labeled into ten land-use and land-cover classes: Annual Crop, Forest, Herbaceous Vegetation, Highway, Industrial, Pasture, Permanent Crop, Residential, River, and Sea/Lake. The images have a spatial resolution of 10 meters.

We use a ResNet50 model pre-trained on ImageNet, modified to accept 13 input channels corresponding to Sentinel-2 spectral bands. The model is fine-tuned with a learning rate of 0.0001 and a batch size of 128. Training runs for up to 100 epochs with early stopping after 5 epochs of no improvement. Input images are normalized using channel-wise mean and standard deviation statistics.

9.2. xBD

xBD [7] is a semantic segmentation dataset for building damage assessment from satellite imagery. The dataset, collected from Maxar’s Open Data Program, has images with a spatial resolution below 0.8 meters. It includes pre- and post-disaster images of hurricanes, floods, wildfires, and earthquakes, making it suitable for evaluating temporal and semantic shifts.

We simplify the damage assessment task into binary segmentation by reassigning damage levels: background (0) and levels 1-2 are grouped, while levels 3-4 form a high-damage class. This minimizes concept drift and ensures a balanced evaluation. We train a U-Net model with a ResNet50 backbone, pre-trained on ImageNet and configured for 3 input channels. Training uses a batch size of 32, a learning rate of 0.001, and runs for up to 50 epochs with early stopping after 5 epochs of no improvement. We reserve 10% of the data for validation and normalize the input images by dividing pixel values by 255.

9.3. FTW

We follow the practices of the original study and use a U-Net model with an EfficientNet-B3 backbone for semantic segmentation on the FTW dataset. The model is configured with 8 input channels and outputs 3 classes: background, field, and field-boundary. We use class weights of [0.04, 0.08, 0.88] to address class imbalance. The learning rate is set to 0.001, and the loss function is cross-entropy. The number of filters is set to 64, and neither the backbone nor the decoder is frozen during training. We set the patience for early stopping to 100 epochs. The images are normalized by dividing pixel values by 3000.

For the classifier, we use logistic regression with a maximum number of iterations set to 500. We train the classifier with 500 ID samples and 1200 WILD samples. The number of clusters is set to 150, calculated as 0.3 times the total number of WILD samples. To reassign labels, we use an ID fraction threshold of 0.1, meaning that a cluster is assigned as OOD if ID samples comprise less than 10% of the total samples in the cluster. The values of 0.3 and 0.1 are determined based on empirical observations gathered from extensive experiments on the xBD and EuroSAT datasets.

Figure 7 provides a visual illustration of the input samples from the WILD set, where the distribution is unknown. It displays the input Sentinel-2 image pair (Window A and Window B) alongside the OOD classifier g ’s prediction scores and the DL model f ’s predictions.

9.4. Introducing Distribution Shifts to EuroSAT and xBD

The combination of EuroSAT and xBD provides a diverse testbed for evaluating distribution shifts. EuroSAT represents regional imagery at medium spatial resolution, while xBD provides global imagery at very high resolution. Their differences in acquisition times, sensor parameters, processing levels, and the tasks they cover—land-cover classification (EuroSAT) and building detection (xBD)—make them complementary. Additionally, EuroSAT focuses on patch-level classification, while xBD involves pixel-level segmentation, enabling evaluations across different problem dimensions.

To evaluate our method, we introduce two types of distribution shifts: **covariate** and **semantic** (described in Table 1). Our approach assumes that purposefully rearranging dataset splits creates measurable shifts between training and testing sets, driven by the logic of the split design.

EuroSAT Distribution Shifts. Figure 6 shows one example from each of EuroSAT’s 10 classes, which differ spa-

tially and semantically. For covariate shifts, we split the dataset by longitude at the midpoint of its spatial extent, using the western half for training and the eastern half for testing. This creates a shift based on spatial proximity.

For semantic shifts, we train the model on 9 classes and test it on the hold-out class, repeating this process for all classes. This ensures the model faces unseen scenarios during testing, providing a robust evaluation of its ability to handle semantic shifts.

xBD Distribution Shifts. Figure 5 illustrates the pre- and post-disaster image pairs in the xBD dataset. Temporal shifts arise from changes occurring between pre- and post-disaster images, while spatial and thematic shifts reflect differences in how disasters impact regions and leave varying degrees of visible marks. Using these inherent characteristics, we design covariate shift experiments for xBD.

10. Design Choices

To better understand the impact of various design choices on the performance of our OOD detection method, we conduct a series of ablation studies. Specifically, we explore four key factors: (1) the choice of layer from which to extract feature representations (Section 10.1), (2) the method used to downsample these feature maps (Section 10.2), (3) the type of binary classifier g used to distinguish between surrogate-ID and surrogate-OOD samples (Section 10.3), and (4) the selection of hyperparameters k and T for surrogate label assignment (Section 10.4).

10.1. Which Layer?

Selecting the appropriate layer for activation extraction is crucial for accurate OOD detection. Prior works have emphasized the importance of this choice. For example, ASH achieves optimal performance on later layers like the penultimate layer, as earlier layers suffer from significant performance degradation during pruning [4]. Similarly, ReAct performs best on the penultimate layer, where more distinctive patterns between ID and OOD data emerge [24]. NAP-based OOD detection further highlights the variability in layer effectiveness, dynamically selecting top-performing layers based on validation accuracy [20]. Consistent with these findings, we observe that no single layer is universally optimal across all settings.

We benchmark FPR95 scores for OOD detection across the first convolutional layer, eight randomly selected intermediate layers, and the last convolutional layer. As shown in Table 3 for the EuroSAT dataset and Table 4 for the xBD dataset, layer performance varies significantly. While late layers often perform well, early and middle layers frequently give competitive results, depending on the dataset and task. Based on these findings, we select the best-performing layer for each experiment.

For the large-scale FTW dataset, the lack of distribution shift information prevents evaluation of layer-specific performance for OOD detection. Therefore, based on the observation that many layer benchmarks perform optimally for middle layers, we select a middle convolutional layer, specifically ‘decoder.blocks.0.conv1’ from the U-Net model with an EfficientNet-B3 backbone.

10.2. Which Downsampling Method?

Having identified the layer to extract internal activations from, the next step is to look into the effect of downsampling these activations, which can reduce computational complexity and noise while retaining essential features for OOD detection. We explored four methods:

1. **Mean and standard deviation (*Mean Std*):** Computes the mean and standard deviation across the spatial dimensions (H, W) for each channel, providing two descriptive statistics per feature channel.
2. **Average pooling (*Avg Pool*):** Global average pooling was applied, reducing the activation to a single representative value per channel by averaging all spatial values.
3. **Max pooling (*Max Pool*):** Uses global max pooling to retain the maximum value from each spatial dimension, capturing the most prominent feature in each channel.
4. **PCA-based reduction (*PCA*):** Applies Principal Component Analysis (PCA) to reshape the activation map into a vector and projects it into a lower-dimensional space with 10 components.

We summarize the OOD detection performance across all experiments on the EuroSAT and xBD datasets under different downsampling methods in Table 5, using the FPR95 metric. Max pooling consistently achieves the best performance across the majority of experiments, making it the preferred approach. We attribute its performance to its ability to retain the most prominent features in each channel, filtering out less significant information. This focus on salient patterns likely enhances the OOD classifier’s capacity to distinguish between ID and OOD samples.

10.3. Which Classifier?

The next key design choice is the selection of the binary classifier g , used to distinguish between surrogate-ID and surrogate-OOD samples based on their feature representations. The results, summarized in Table 6, report the mean performance across all experimental measurements along with the standard error of the mean to represent confidence intervals. We select Logistic Regression as it provides the best tradeoff between classification accuracy and prediction time. This balance is essential for scaling up the method, where both efficiency and accuracy are critical.

10.4. Surrogate Label Assignment: Hyperparameter Search for k and T

TARDIS relies on a clustering-based approach in the activation space to assign surrogate ID and surrogate OOD labels. This process requires selecting two key parameters: the number of clusters (k) to segment the activation space, and the ID fraction threshold (T), which determines whether a cluster is assigned as surrogate ID or surrogate OOD. Clusters with an ID fraction above T are assigned as surrogate ID, and those below T are assigned as surrogate OOD.

The underlying assumption is that samples with similar distributions lie closer in the activation space than those from dissimilar distributions. Effectively segmenting the activation space is critical, as the distributions of WILD samples are unknown during deployment. Segmenting nearby activations and correctly assigning clusters to surrogate ID or OOD makes the choice of k and T crucial for accurate OOD detection.

To develop insights into selecting k and T , we conduct controlled experiments on EuroSAT and xBD, where ID and OOD labels are known. In these experiments, we treat OOD labels as WILD and apply our clustering-based surrogate label assignment logic. By holding back the ground-truth WILD labels, we simulate real-world conditions while being able to evaluate the results against known labels.

The primary goal is to understand how to choose k and T , and whether there are patterns we can extrapolate to real-life deployment. For this, we calculate the ratio of k to the total number of training samples and evaluate its effect on OOD detection performance (Accuracy, FPR95, and AUROC). We plot these metrics against the ratio of k /total training samples, increasing k until the ratio reaches 1. Theoretically, OOD detection improves with more clusters as this enables finer-grained segmentation of the activation space, reducing the risk of including anomalies in ID clusters.

To establish a theoretical maximum (oracle performance), we also evaluate OOD classification with known ID and OOD labels, bypassing the need for clustering. This oracle performance is represented by horizontal dashed lines in Figures 8 and 9 (upper plots). The results for two representative experiments—one from EuroSAT and one from xBD—since all experiments show similar trends. We observe that the performance approaches the oracle boundaries when k is approximately 0.3 times the total number of training samples. While performance improves as k increases, a trade-off is required between performance and walltime as well as computational complexity. Based on this trade-off, we set k to 0.3 for all experiments, including the large-scale deployment on FTW. Furthermore, we observe that our method is not highly sensitive to T . As a result, we fix T to 0.1 for all experiments, which is the value used in this initial investigation. We use the Optuna library

to implement a Bayesian-based search algorithm. The composite objective function, which we minimize to determine the optimal number of clusters and ID fraction threshold, is detailed in Section 4.

Lastly, the gradual improvement in OOD detection performance with increasing k supports our assumption that samples with similar distributions lie closer in the activation space than those with dissimilar distributions. The absence of degradation in performance further underscores the importance of activation-level clustering as a reliable proxy for domain estimation based on neighboring samples.

We set k and T as described and use t-SNE in the lower plots of Figures 8 and 9 to reduce the dimensionality of the activation spaces to 2D for visualization. When ID and OOD labels are known, the t-SNE plots show that only a small fraction of labels changes from the original labels. This demonstrates the effectiveness of the surrogate label assignment process described above.

11. Additional Experimental Results

In Figure 10, we show the predictions of the DL model f and the OOD classifier g , along with the ground truth class and distribution annotations for the EuroSAT experiment, where Forest serves as the OOD class. The model f trains on 9 classes (excluding Forest) and tests on Forest. The first row shows correct predictions by f , while the second row shows incorrect predictions. Even when f makes misclassifications, g accurately quantifies the distribution shifts in most cases. The performance of f on the test set is not directly measurable since the test uses a single unseen class. We report the performance of g as: Accuracy = 0.9325, ROC AUC = 0.9886, and FPR95 = 0.0619.

For xBD, we present results where f trains on Hurricane Matthew (ID, Figure 11) and tests on Mexico Earthquake (OOD, Figure 12). Comparing the input images and masks between ID and OOD shows that even when f performs suboptimally, g effectively quantifies the distribution shifts. The performance of f on the test set is: Multiclass Accuracy = 0.7690 and Multiclass Jaccard Index = 0.6248. We attribute f 's suboptimal prediction performance to the significant distribution shift between the training (Hurricane Matthew) and testing (Mexico Earthquake) datasets. The performance of g is: Accuracy = 0.9806, ROC AUC = 0.9986, and FPR95 = 0.0.

Experiment	2/217	8/217	16/217	38/217	43/217	48/217	118/217	139/217	199/217	211/217
Forest	0.0625	0.01	0.00	0.00	0.00	0.00	0.0078	0.0156	0.0391	0.0391
HerbVeg	0.2857	0.22	0.3095	0.22	0.2778	0.1429	0.07	0.1032	0.2460	0.2778
Highway	0.8319	0.5462	0.6218	0.3529	0.3613	0.21	0.12	0.0840	0.1765	0.2437
Industrial	0.2406	0.01	0.0376	0.0226	0.0226	0.00	0.0150	0.0226	0.0376	0.0075
Pasture	0.1288	0.0909	0.12	0.1364	0.0985	0.03	0.0833	0.0227	0.1212	0.2273
PermCrop	0.3554	0.2975	0.3140	0.2397	0.2314	0.14	0.12	0.1322	0.2066	0.1653
Residential	0.2960	0.00	0.0160	0.0240	0.00	0.00	0.00	0.0160	0.0400	0.0480
River	0.4688	0.07	0.2031	0.03	0.0938	0.0234	0.0078	0.0078	0.0625	0.0859
SeaLake	0.00	0.00	0.00	0.00	0.00	0.00	0.00	0.00	0.00	0.00
AnnualCrop	0.2879	0.00	0.0303	0.0606	0.0530	0.02	0.0379	0.0152	0.0682	0.0758
SpatialSplit	0.3182	0.20	0.4773	0.15	0.1970	0.0909	0.2197	0.2273	0.6364	0.7652
Avg \pm Stdev	0.2978 \pm 0.2223	0.1313 \pm 0.1729	0.1936 \pm 0.2133	0.1124 \pm 0.1176	0.1214 \pm 0.1264	0.0597 \pm 0.0741	0.0620 \pm 0.0696	0.0588 \pm 0.0712	0.1486 \pm 0.1801	0.1760 \pm 0.2185

Table 3. FPR95 scores for OOD detection for experiments on EuroSAT dataset across the first convolutional layer, eight randomly selected layers, and the last convolutional layer. Notation in the header (e.g., X/Y) refers to the 'layer number / total number of layers.' The last row, labeled 'Avg \pm Stdev,' provides the mean \pm standard deviation of the scores for each layer across all experiments.

Experiment	3/223	60/223	112/223	146/223	148/223	162/223	176/223	187/223	208/223	216/223
Nepal Flooding	1.0000	0.09	0.6986	0.7534	0.6986	0.7397	0.46	0.8767	0.8356	0.8493
- Midwest Flooding										
Santa Rosa Wildfire	0.5000	0.36	0.36	0.7222	0.6389	0.6389	0.6944	0.6111	0.58	0.9167
- Woolsey Fire										
Hurricane Matthew	0.3023	0.06	0.3488	0.4419	0.4884	0.32	0.1163	0.3488	0.2791	0.4419
- Nepal Flooding										
Hurricane Matthew	0.11	0.1471	0.2353	0.6471	0.4118	0.50	0.3235	0.4706	0.6471	0.9706
- Mexico Earthquake										
Portugal Wildfire (Pre-Post)	0.38	0.9583	0.3889	0.8472	0.8750	0.9167	0.9722	0.77	0.9861	0.8472
Mean \pm Stdev	0.4585 \pm 0.3343	0.3231 \pm 0.3740	0.4063 \pm 0.1735	0.6824 \pm 0.1524	0.6225 \pm 0.1818	0.6231 \pm 0.2275	0.5133 \pm 0.3316	0.6154 \pm 0.2146	0.6656 \pm 0.2686	0.8051 \pm 0.2095

Table 4. FPR95 scores for OOD detection experiments on the xBD dataset across the first convolutional layer, eight randomly selected layers, and the last convolutional layer. Notation in the header (e.g., X/Y) refers to the 'layer number / total number of layers.' The last row, labeled 'Avg \pm Stdev,' provides the mean and standard deviation of the scores for each layer across all experiments.



Figure 5. Examples from the xBD dataset, illustrating pre- and post-disaster images. These samples demonstrate the temporal and semantic differences between pre- and post-disaster scenes, highlighting the challenges posed by distribution shifts.



Figure 6. Examples from the dataset, with one sample from each class. These images highlight the spatial and semantic distinctions across classes.

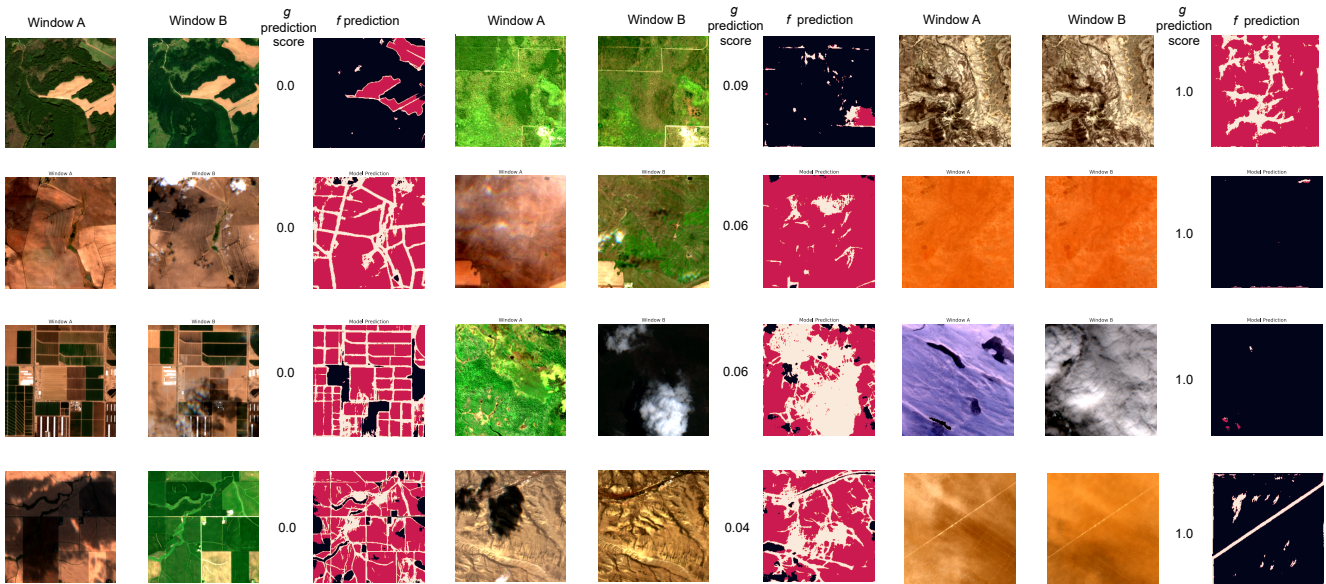


Figure 7. The input samples are from the WILD set, where the distribution is unknown. The figure shows Sentinel-2 images at two different times (planting season and harvesting season — Window A and Window B). When these windows are fed together into f , the model outputs both the segmentation prediction and the OOD classifier g 's prediction score.

Experiment	Avg Pool	Mean Std	Max Pool	PCA
Forest	<i>0.0859</i>	0.4297	0.0234	0.8750
HerbaceousVegetation	<i>0.2937</i>	0.8651	0.2698	0.9921
Highway	0.7899	<i>0.7311</i>	0.7059	0.9412
Industrial	<i>0.1880</i>	0.2857	0.0526	0.9925
Pasture	0.0909	0.6970	<i>0.2576</i>	0.9924
PermanentCrop	0.3058	0.9008	<i>0.4215</i>	0.9669
Residential	<i>0.2640</i>	0.6640	0.2160	0.8480
River	<i>0.4922</i>	0.6172	0.1563	0.9922
SeaLake	0.0000	0.0313	0.0000	0.9766
AnnualCrop	<i>0.2500</i>	0.7576	0.0455	0.9924
SpatialSplit	<i>0.3182</i>	0.5379	0.3030	0.9848
Nepal Flooding - Midwest Flooding	0.0000	<i>0.6575</i>	0.9452	0.9726
Hurricane Matthew - Nepal Flooding	0.0233	0.9070	<i>0.5581</i>	0.9535
Hurricane Matthew - Mexico Earthquake	0.0588	0.9118	<i>0.5882</i>	1.0000
Portugal Wildfire Pre - Portugal Wildfire Post	<i>0.9028</i>	0.9861	0.8472	1.0000

Table 5. FPR95 scores for OOD detection across different downsampling methods. The table compares performances of average pooling, mean and standard deviation pooling, max pooling, and PCA for various experiments. Bold values indicate the best performance for each experiment, while italicized values represent the second-best performance.

Classifier	Accuracy \uparrow	ROC_AUC \uparrow	FPR95 \downarrow	Prediction Time (ms/sample)
KNeighbors	92.23 \pm 0.81	86.85 \pm 1.07	<i>38.79 \pm 2.02</i>	73.00 \pm 8.00
GaussianNB	84.28 \pm 1.04	89.37 \pm 0.91	32.89 \pm 1.89	4.00 \pm 1.00
DecisionTree	91.21 \pm 0.93	77.43 \pm 1.20	78.81 \pm 2.41	2.00 \pm 1.00
ExtraTrees	93.30 \pm 0.67	91.29 \pm 0.83	<i>28.53 \pm 1.94</i>	12.00 \pm 3.00
LogisticRegression	87.67 \pm 1.00	<i>93.33 \pm 0.87</i>	27.20 \pm 1.98	<i>3.00 \pm 1.00</i>
SVC	91.54 \pm 0.90	94.26 \pm 0.72	19.87 \pm 1.85	67.00 \pm 12.00
RandomForestUnbalanced	92.54 \pm 0.82	91.24 \pm 0.80	30.98 \pm 1.95	9.00 \pm 2.00
RandomForest	<i>92.76 \pm 0.75</i>	91.11 \pm 0.84	30.24 \pm 1.91	8.00 \pm 2.00
AdaBoost	92.85 \pm 0.79	92.03 \pm 0.82	29.84 \pm 1.89	11.00 \pm 3.00
GradientBoosting	92.92 \pm 0.81	93.11 \pm 0.85	30.47 \pm 1.88	7.00 \pm 2.00

Table 6. Benchmark results of classifiers g , including Accuracy, ROC_AUC, FPR95, and prediction time. Values are reported as mean \pm SEM over all experiments on EuroSAT and xBD. Bold indicates the best performance, and italics indicate the second-best performance. Prediction time is reported in milliseconds (ms/sample).

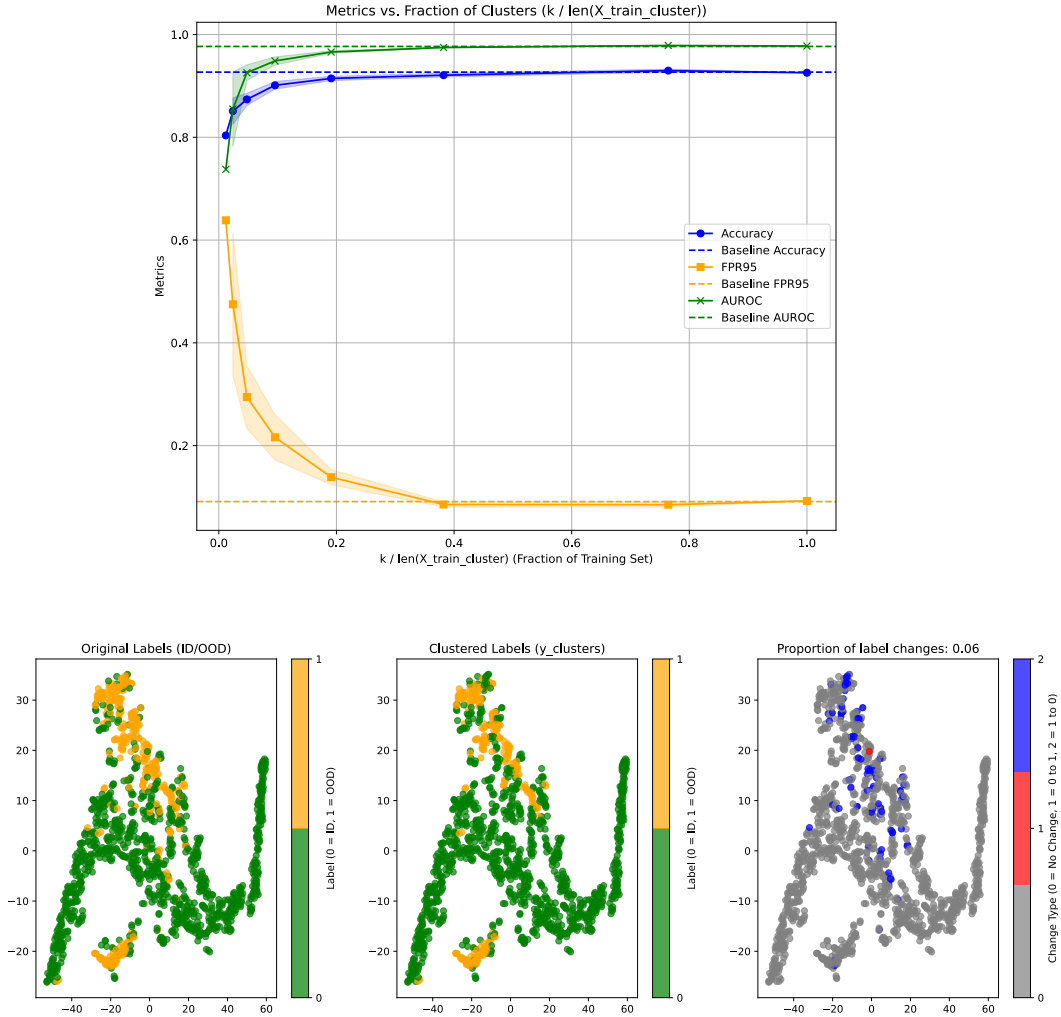


Figure 8. EuroSAT Pasture experiment on surrogate label assignment. The upper plot shows the performance metrics (Accuracy, FPR95, AUROC) for the oracle classifier g_{oracle} and the surrogate classifier g^* as the ratio of clusters to training samples $k/\text{len}(X_{\text{train}})$ increases. As k grows, g^* gradually improves and approaches the performance of g_{oracle} . The lower plot visualizes the feature space before and after clustering, showing how original ID and OOD labels are reassigned to surrogate ID and OOD labels based on the clustering logic.

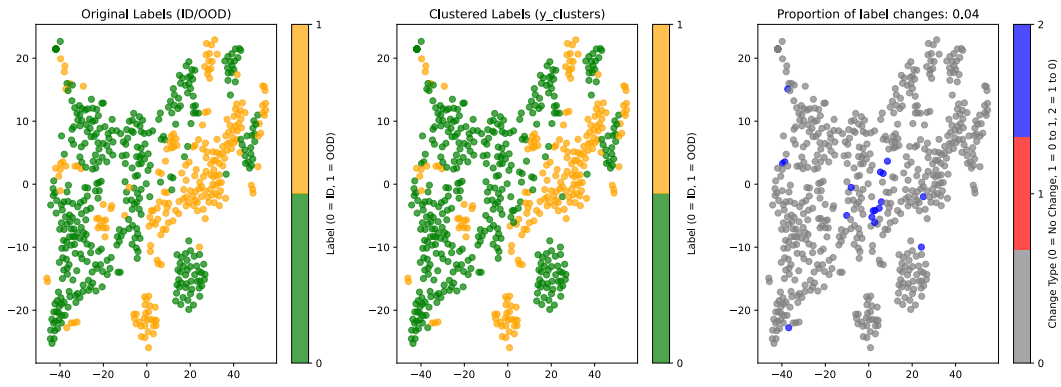
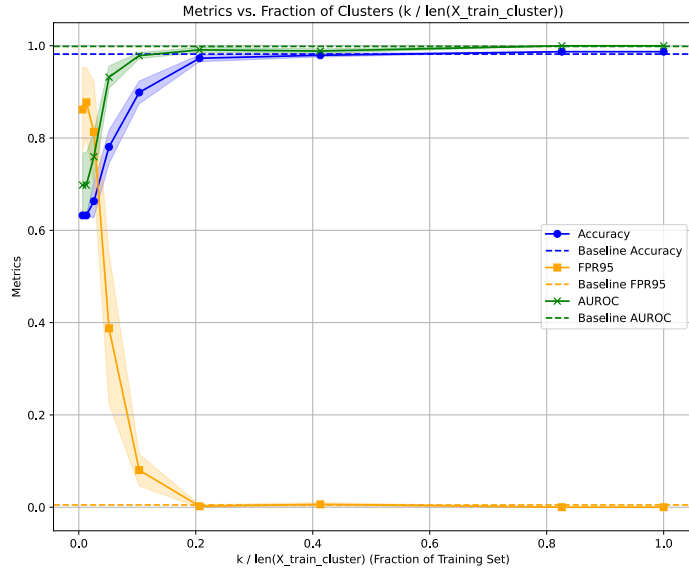


Figure 9. xBD Nepal Flooding-Midwest Flooding disaster experiment on surrogate label assignment. The upper plot shows the performance metrics (Accuracy, FPR95, AUROC) for the oracle classifier g_{oracle} and the surrogate classifier g^* as the ratio of clusters to training samples $k/\text{len}(X_{\text{train}})$ increases. As k grows, g^* gradually improves and approaches the performance of g_{oracle} . The lower plot visualizes the feature space before and after clustering, showing how original ID and OOD labels are reassigned to surrogate ID and OOD labels based on the clustering logic.

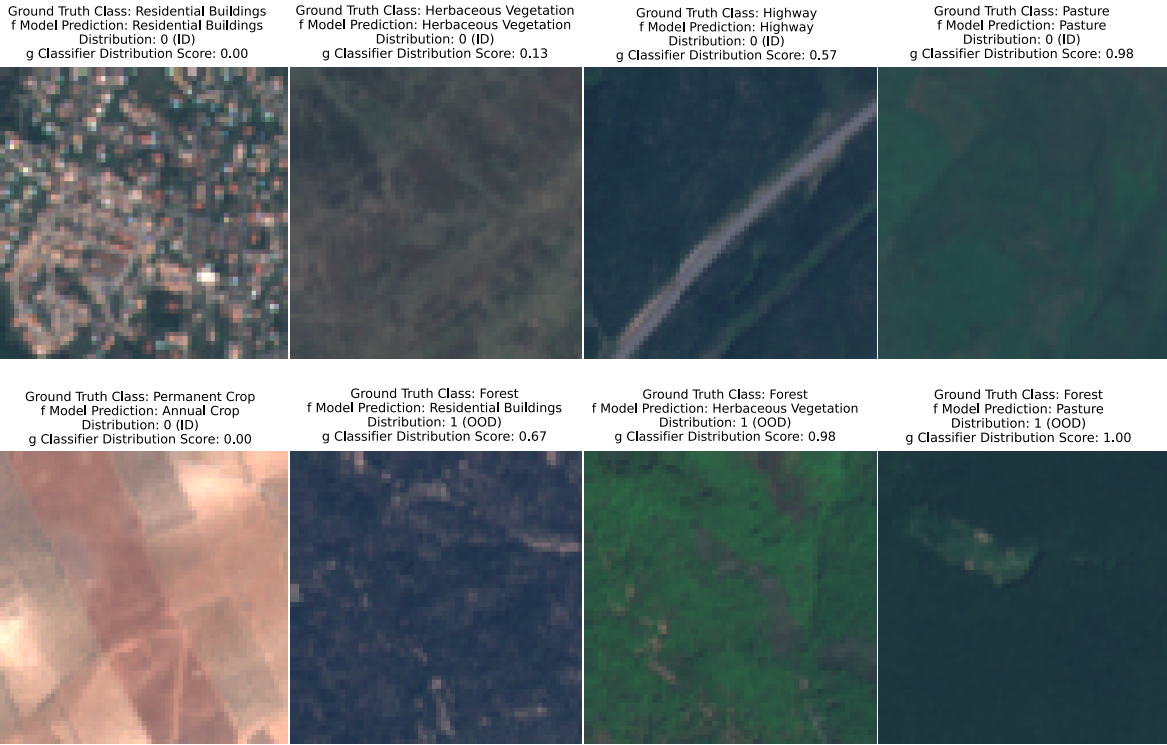


Figure 10. EuroSAT experiment with Forest as the OOD class. The figure shows predictions of the DL model f and the OOD classifier g , along with the ground truth class and distribution annotations. The first row represents samples where f makes correct class predictions, while the second row represents samples where f makes incorrect predictions. For each sample, we report both the ground truth distribution and the predicted distribution from g .

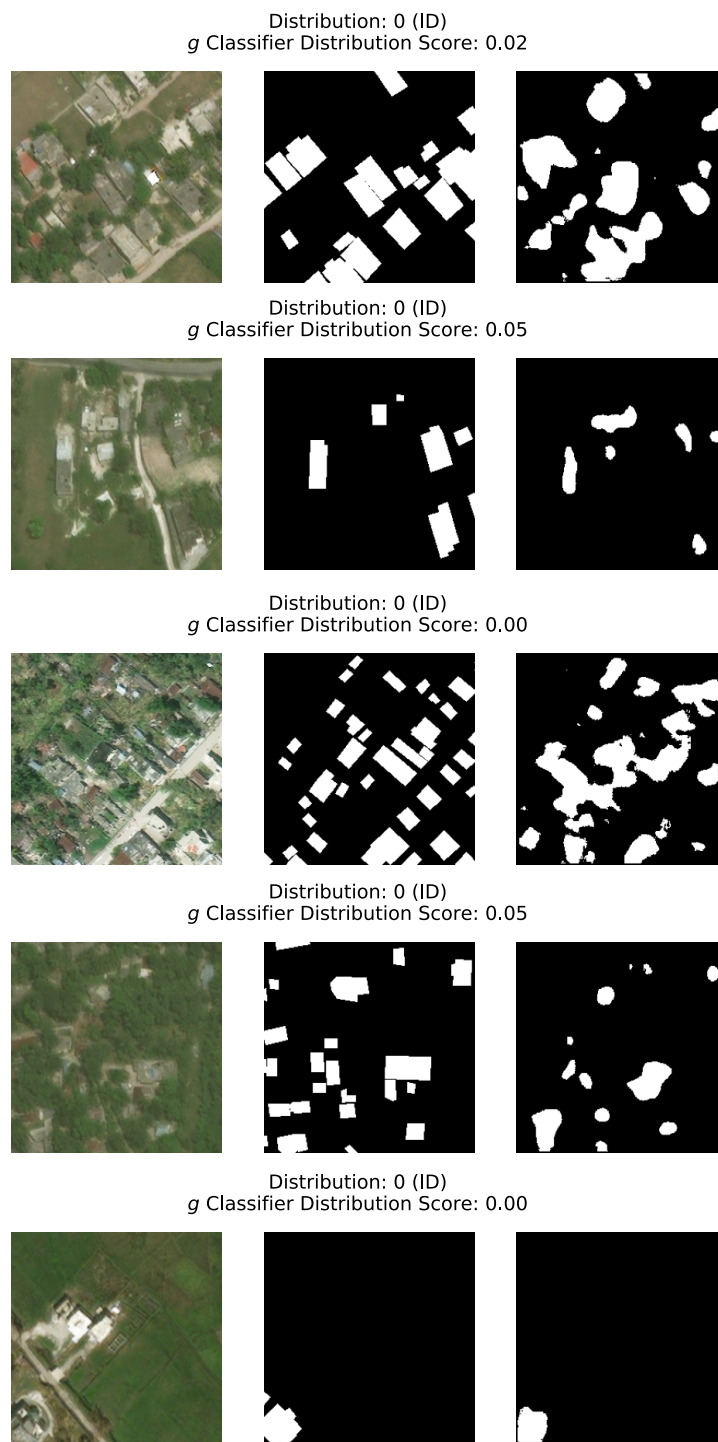


Figure 11. xBD experiment with Hurricane Matthew as the ID samples. The figure shows the annotations and predictions of the DL model f and the OOD classifier g . For each sample, we present f 's predicted class and g 's predicted distribution, along with the ground truth annotations.

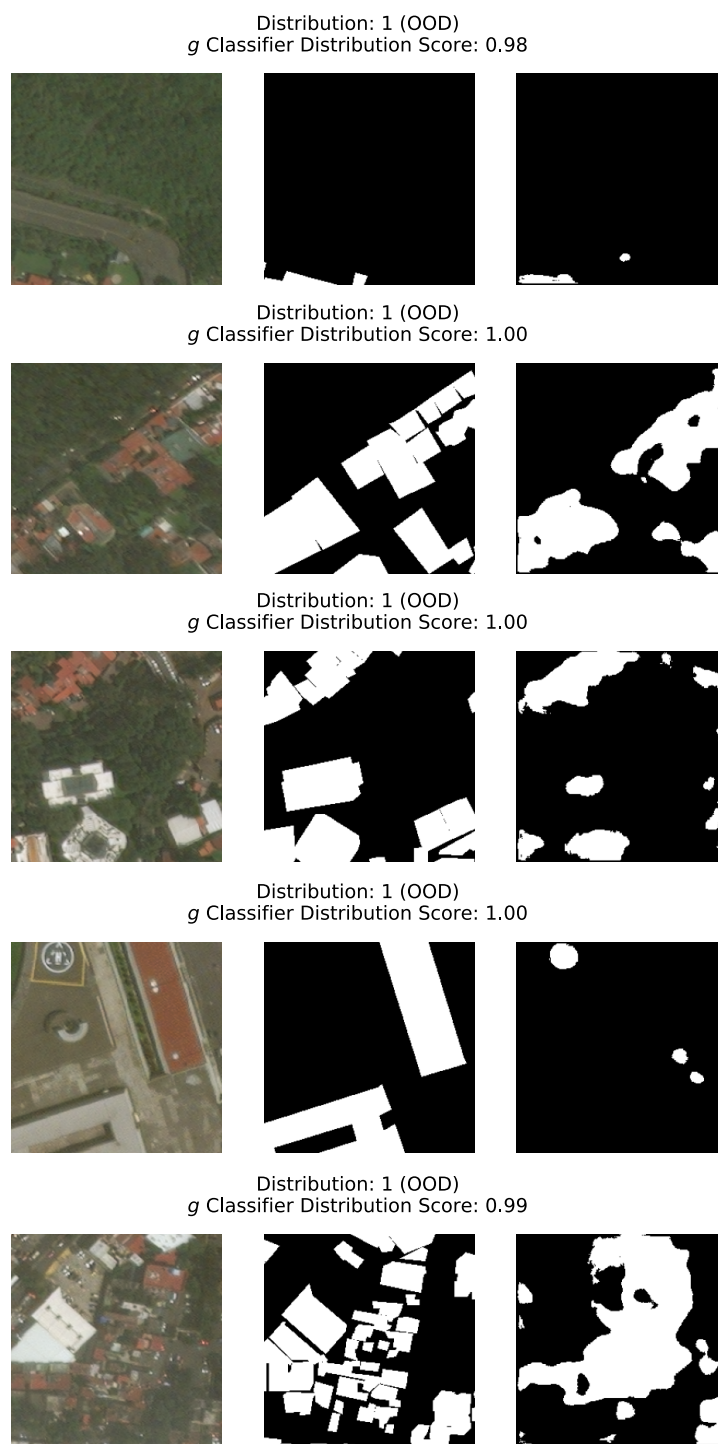


Figure 12. xBD experiment with Mexico Earthquake as the OOD samples. The figure shows the annotations and predictions of the DL model f and the OOD classifier g . For each sample, we present f 's predicted class and g 's predicted distribution, along with the ground truth annotations.